

# $\gamma$ Cassiopeiae revisited by spectrally resolved interferometry

Ph. Stee<sup>1</sup>, F.X. de Araújo<sup>2</sup>, F. Vakili<sup>1</sup>, D. Mourard<sup>1</sup>, L. Arnold<sup>1</sup>, D. Bonneau<sup>1</sup>, F. Morand<sup>1</sup>, and I. Tallon-Bosc<sup>3</sup>

<sup>1</sup> Observatoire de la Côte d'Azur, Département Fresnel, CNRS URA 1361, F-06460 Saint Vallier de Thiey, France

<sup>2</sup> CNPq-Observatório Nacional, DAGE, Rua General Bruce 586, Rio de Janeiro, CEP 20291, Brazil

<sup>3</sup> Observatoire de Lyon, F-69561 Saint Genis Laval Cedex, France

Received 15 November 1994 / Accepted 31 January 1995

**Abstract.** We present a model for the Be star  $\gamma$  Cassiopeiae which is based on spectroscopic and interferometric data collected with the Grand Interféromètre à 2 Télescopes (GI2T) in southern France. Our model assumes a standard radiation-driven wind in the polar regions. Using a parametrized and axisymmetric scheme we deduce the wind for other stellar latitudes. The comparison of computed and observed  $H\alpha$  profiles during October and November 1993, together with the interferometric measurements, allows us to constrain both the density and velocity relationships present in the equatorial plane. For the first time we have shown that a model of a radiative wind driven by optically thin lines can account well for our angular/spectral resolution data.

**Key words:** stars: circumstellar matter – stars: Be – stars: individual ( $\gamma$  Cas) – lines: profile – stars: mass loss – techniques: interferometric

## 1. Introduction

$\gamma$  Cas is certainly one of the best studied Be stars of the northern hemisphere. Since the ad-hoc scenario extensively developed by Poeckert and Marlborough (hereafter PM, 1978), numerous models which attempted to reproduce isolated characteristics of Be stars have been proposed (Waters & Marlborough 1992, and references therein). A few of these models are physically consistent in the sense that they start from the hydrodynamic equations in order to provide the density distribution and the velocity fields throughout the envelope. Most of the other models are ad-hoc and try to fit a few observable features by constraining as many free parameters as possible. In this paper we propose a strategy which lies between these two different approaches for solving the problem of the too large terminal speeds of winds driven by strong lines (see also Stee & Araújo 1994; hereafter SA).

### 1.1. The Be phenomenon

The Be phenomenon is characterized by the presence of emission lines in the optical to the near IR region of the spectrum. This emission originates in an extended and fast moving atmosphere around the star. The high luminosity of the star produces a hot stellar wind responsible for the spectacular broadening of both optical and UV lines and displaces their central wavelengths. In addition, the fast stellar rotation strongly broadens the photospheric lines. Unsurprisingly, the line formation regions are not spherically distributed around the star. It seems that the UV lines are absorbed in a medium where the hydrogen density is low and which expands with velocities as high as 2000  $\text{kms}^{-1}$ . This is called the “polar wind” because it probably originates from the polar regions (e.g. Marlborough 1987). On the other hand, the equatorial region seems to be more dense and is characterized by a lower radial expansion (i.e. 100-200  $\text{kms}^{-1}$ ) and a high rotation where the Balmer lines are produced (PM, Waters 1986; Waters et al. 1987; Waters & Marlborough 1992). The third major characteristic of the Be phenomenon is related to the variability of these stars. This variability can be spectroscopic (Slettebak & Snow 1978; Dachs et al. 1986; Doazan et al. 1987; Floquet et al. 1992; Hubert 1994), photometric (Walker 1953; Doazan et al. 1986; Pavloski 1987; Hubert 1994) or morphologic (Percheron et al. 1994); the time scales range from hours to years. Detailed reviews are given by Doazan (1982) and Slettebak (1988). Furthermore a Be star can undergo different phases exhibiting normal B star features (i.e. the absence of emission lines) or Be-shell profiles. The links between these different aspects are as yet not clear. Following the model of PM, a number of authors have developed ad-hoc models in order to explain various observational characteristics of Be stars. For instance Telting et al. (1993) try to explain V/R variations and the slope of the IR continuum in terms of an expanding/contracting spherical shell model or a non-axisymmetric disc model. Telting & Kaper (1994) used a one-armed oscillation in order to explain periodic variability in UV absorption lines. Nevertheless, there is no physical model which can produce this kind of variability, primarily because of the complexity of developing

Send offprint requests to: Ph. Stee

a three dimensional non-stationary hydrodynamic model.

Owing to the high luminosity of the underlying star the equatorial and polar regions are almost fully ionized and produce free-free and free-bound emission corresponding to an IR excess. The free electrons are also responsible for the high intrinsic linear polarization observed in many Be stars. This polarization is direct evidence for the oblateness of the envelope, also called the “equatorial disc”. Using long baseline interferometry in the visible, Mourard et al. (1989) found that the data roughly agree with the PM disc model of a rotating envelope. More recently Quirrenbach et al. (1994) concluded that the MkIII data rules out any spherical or nearly spherical models (Doazan 1987).

During the last decade many authors have tried to model the physics of Be star envelopes in the context of radiatively driven wind. Poe and Friend (1986) used the pionnering work by Castor et al. (1975; hereafter CAK). Araújo & Freitas Pacheco (1989) developed a two-dimensional treatment of the wind including viscosity and the effects of the stellar rotation. More recently Bjorkmann & Cassinelli (1993) proposed a model where a meridional flow compresses and confines the equatorial material in a very thin disk. Owocki et al. 1994 qualitatively confirmed their results in a non-stationary hydrodynamical simulation. The compression which occurs in their model is large enough to produce a shock which heats the flow and superionizes the wind. This temperature enhancement can explain observations of EUV and soft X-ray emission and indicates that the CIV ions are concentrated towards the equator. Nevertheless, such a thin disk with an opening angle of a few degrees is unlikely to produce strong emission profiles, especially the shell features often observed among the Be stars.

A challenging problem which has yet to be solved for most radiative wind models is the excessive width of the Balmer emission line profiles. Recent quantitative computations by SA, who found a separation of  $2000 \text{ km s}^{-1}$  between the V and R peaks of  $H\alpha$ , reinforce this conclusion. In order to overcome this difficulty, SA suggest the possibility of a flow which is essentially driven by a large number of optically thin lines in the equatorial region (see also Lamers 1986; Marlborough 1987; Boyd & Marlborough 1991). Such a wind would have a lower terminal velocity and would produce emission line profiles that were less broadened. This hypothesis is supported by IUE spectra of Be stars which show a very large number of optically thin lines. Recently Chen & Marlborough (1994) presented a wind driven by optically thin lines. But due to numerical problems, they could not directly obtain a solution when the radiative parameter force  $\alpha$  was smaller than 0.3. Therefore they used a parametric form for the radiative force. We recall that the  $\alpha$  parameter represents the fraction of optically thick lines in the total number of driving lines.

In this paper we adopt the following approach. First we presume that the physical conditions in the “polar-wind” are well represented by a CAK-type wind model. Subsequently we intro-

**Table 1.** Parameters for  $\gamma$  Cassiopeiae

$\gamma$ Cas	
Spectral type	B0.5IVe
Effective temperature	25000 K
Mass	$16 M_{\odot}$
Radius	$10 R_{\odot}$
Luminosity	$3.510^4 L_{\odot}$
$V \sin i$	$230 \text{ km s}^{-1}$
Inclination angle $i$	$45^{\circ}$

duce a parametrized model for other stellar latitudes. By choosing adequate parameters, we obtain  $H\alpha$  line profiles, intensity maps in  $H\alpha$  and at different Doppler-shifts across  $H\alpha$  which agree with the data obtained from the Grand Interféromètre à 2 Télescopes (GI2T) observations. Finally we have reproduced the equatorial terminal velocity and mass flux by using more recent results of a wind model driven by optically thin lines (Araújo 1994).

## 1.2. $\gamma$ Cassiopeiae

The following parameters, summarized in Table 1, have been adopted for  $\gamma$  Cas (HD 5394, B0.5IVe,  $m_v = 2.25$ ):  $v \sin i$  is about  $230 \text{ km s}^{-1}$  (Sletteback 1982), the effective temperature, mass, and radius are respectively 25000 K,  $16 M_{\odot}$ ; and  $10 R_{\odot}$ . The most frequently used value for the inclination angle is  $45^{\circ}$  (Clarke 1990; Quirrenbach et al. 1993). This choice of parameters means  $\gamma$  Cas rotates at 60% of its critical velocity (i.e.  $540 \text{ km s}^{-1}$ ). This implies that  $\gamma$  Cas is a fast rotator but does not spin close to the breakup limit. The aim of this paper is to build for  $\gamma$  Cas a possible scenario mainly based on spectrally-resolved interferometric data and to interpret this scenario in the context of radiative wind models.

The presentation of the paper is as follows. In Sect. 2 we present the journal of observations and outline the data reduction procedure. This reduction provides spectroscopic and interferometric data at the same time. In Sect. 3 we present our hydrodynamic equations for the polar axis and the resulting velocity and density that we have obtained on this axis. On the basis of the polar values, we introduce in Sect. 4 a parametrized scheme for all stellar latitudes. Section 5 presents the “best” model used to build up a possible scenario for  $\gamma$  Cas. In Sect. 6 we compare our results with the data from the GI2T interferometer; the model also predicts the continuum emission and the corresponding visibility. In Sect. 7 we examine the effect of changing the value of model parameters on predicted observables from high angular resolution data. In Sect. 8 we show that a wind driven by optically thin lines can produce the physical conditions that should be present at the equator. In the last section we summarize the main results of our study and discuss the future application of our approach to the understanding of the Be phenomenon.

**Table 2.** Journal of observations of  $\gamma$  Cassiopeiae with the GI2T in November 1993. The first two columns give the number of observation and the gregorian date. The third gives the mean Universal Time for each run. The fourth gives the julian date, the sixth the baseline projected on the sky in meters and the last gives the spatial frequency in cycles/arcsec for the  $H\alpha$  spectral domain.

N	Date	UT	JD	Base	$H\alpha SF$
1	93/10/29	21:57	2449290	15.40	145.1
2	93/11/07	21:22	2449299	15.40	145.1
3	93/11/08	21:18	2449300	20.70	195.4
4	93/11/11	21:06	2449303	20.70	195.4
5	93/11/16	20:47	2449308	28.00	263.7
6	93/11/24	20:11	2449317	37.80	356.1
7	93/11/25	20:07	2449318	51.04	480.8
8	93/11/28	19:55	2449321	29.60	279.3

## 2. Observations and data analysis

### 2.1. Instrumentation

The present study uses spectrally resolved interferometry carried out with the GI2T. The GI2T, which was recently described by Mourard et al. (1994a), is a long-baseline optical interferometer operated at visible wavelengths using apertures of 1.5 meter. It provides spectra with interference fringes. The corresponding angular resolution approaches 1 milliarcsecond, including a spectral resolution of about 0.1 nm. It therefore makes it possible to study the dynamics of Be star envelopes by comparing the interferometric signals across emission lines and the nearby continuum. This unique property enabled Mourard et al. (1989) to reveal the rotation of the envelope of  $\gamma$  Cas by comparing the GI2T data to the existing model of PM. The interpretation of these initial observations was somewhat hampered by the lack of appropriate envelope models. By appropriate, we mean models which produce observables, as intensity maps and their corresponding two dimensional Fourier transforms, that can be directly compared to interferometric data.

### 2.2. Observations

We observed  $\gamma$  Cas during 8 nights in October and November 1993 (Table 2.) We used 6 different interferometric baselines ranging from 15 to 51 meters. The interferometric signal was recorded on average for 1 hour at each baseline around the meridian transit. Because the GI2T baseline has a fixed north-south orientation, we obtained the spatial power spectrum of  $\gamma$  Cas on 6 different samples in the almost north-south directions only. The data were recorded with the CP40 photon counting detector (Blazit 1987; Foy 1988) and later processed. The different steps of raw data correction and spectral calibration follow the procedures described by Vakili et al. (1994).

### 2.3. Data reduction

We reduced the GI2T data following the spectral density method developed for large aperture interferometry (Mourard et al. 1994b). Three different processing routines have been used on the  $\gamma$  Cas data.

#### 2.3.1. Autocorrelation method

We compute the ensemble average autocorrelation of short exposures. Each short exposure is a spectrally dispersed interferogram containing both spectroscopic and angular resolution information. Each interferogram is divided into 2 spectral channels: one is centred on the  $H\alpha$  line and the other on the blue or redward continuum next to the line. The visibility in each channel is then measured by Fourier transforming separately the resulting autocorrelation. If we denote  $V_l$  and  $V_c$  to be the visibilities in the line and in the continuum, our measurement  $M_a$  can be expressed as

$$M_a = \frac{V_l}{V_c}, \quad (1)$$

where  $M_a$  is the line visibility referenced by the continuum visibility. This quantity is in principle independent of seeing and instrumental noise and its standard deviation is given by:

$$dM_a = M_a \cdot \left( \frac{dV_l}{V_l} + \frac{dV_c}{V_c} \right). \quad (2)$$

#### 2.3.2. Cross-correlation

We cross-correlate a wide spectral channel taken in the continuum with a channel centered on the line. By using flat-fielded spectra around  $H\alpha$ , we determine the total width of the emission line. We set the line channel for the cross-correlation to this width. In order to calibrate this visibility, noted  $V_l$ , we also compute the cross-correlation between two continuum bands having the same width as for the cross correlation of continuum versus line. It can easily be shown that:

$$V_l = \sqrt{V_c \cdot V_l} \text{ and } V_2 = \sqrt{V_c \cdot V_c} = V_c. \quad (3)$$

In order to obtain the same measurement as previously, we have to compute

$$M_c = \left( \frac{V_1}{V_2} \right)^2 = \frac{V_l}{V_c} \text{ with } dM_c = 2 \cdot M_c \cdot \left( \frac{dV_1}{V_1} + \frac{dV_2}{V_2} \right) \quad (4)$$

#### 2.3.3. Spectral analysis of the complex visibility

In this case, we compute the cross-correlation of a wide continuum channel with a series of narrow channels through the emission line. However we leave a spectral gap between these continuum and line channels. Next we shift both channels redward by a spectral step equal to the line channel width. Thus we obtain a series of cross-correlations between the continuum and narrow channels across the line. The analysis of the complex Fourier transform of this integration gives us both the modulus of the visibility as in the previous case but also the phase difference between the two channels.

**Table 3.** Visibility measurement obtained on the  $H\alpha$  line from the GI2T. N is the number of observation given in Table 2, SF is the spatial frequency in cycles/arcsec and  $M_a$  and  $M_c$  are the measurements as described in Sects. 2.3.1 and 2.3.2.

N	SF	$M_a$	$\Delta M_a$	$M_c$	$\Delta M_c$
1	145.1	0.681	0.096	0.786	0.161
2	145.1	0.674	0.106	0.663	0.200
3	195.4	0.568	0.045	0.690	0.149
4	195.4	0.616	0.154	0.663	0.290
5	263.7	0.535	0.167	0.526	0.206
6	356.1	0.531	0.132	0.495	0.150
7	480.8	0.477	0.097	0.499	0.140
8	279.3	0.527	0.135	0.498	0.152

#### 2.4. Discussion on the results from interferometry

The visibility measurements for the  $H\alpha$  domain are given in Table 3 as a function of the spatial frequency. We used the methods of data analysis described in Sects. 2.3.1 and 2.3.2 for estimating the visibility moduli as a function of baseline (Fig. 10). Error bars per visibility point are quoted by measuring the noise level from power or cross-spectra of interferograms averaged over the entire set of data per baseline. The average error is on the order of 15% to 20% per visibility point. Note that short baselines are not sampled with the GI2T, essentially due to the physical size of the telescopes and the width of the central beam combination laboratory. As it will become clear in Sect. 7 the problem of this spatial frequency gap is overcome using the properties of our modelling approach of the visibility function. Table 4 corresponds to the results from the processing described in Sect. 2.3.3. Since the cross-spectrum analysis between the continuum and narrow spectral bands across the  $H\alpha$  line is handicapped by the small number of photons in the latter it is indispensable to select a set of data with the higher signal to noise ratio. We choose the 20.7 and 37.8 meter baselines for this purpose (see Fig. 15 and Fig. 16).

### 3. Physics in the polar axis

As already emphasized in Sect. 1.1, we assume that the physics of the polar wind is well represented by a CAK-type stellar wind model. This implies that we must solve both the expansion equation in the polar direction,

$$v_r \frac{\partial v_r}{\partial r} + \frac{1}{\rho} \frac{\partial P}{\partial r} + \frac{GM(1-\Gamma)}{r^2} - \frac{1}{\rho} F^l = 0, \quad (5)$$

and the continuity equation,

$$\Phi = r^2 \rho v_r. \quad (6)$$

In these expressions  $P$  is the gas pressure,  $M$  is the stellar mass,  $G$  is the gravitational constant and  $\Gamma$  is the ratio between electronic radiative acceleration and gravity.  $F^l$  is the radiative

**Table 4.** Visibility measurement across the  $H\alpha$  line profile for the 20.7 and 37.8 meter baselines from the cross spectrum analysis.  $\lambda$  is the central wavelength of the narrow bandwidth (4 Å), M1 and M2 are the corresponding moduli of the visibilities and  $\Delta M1$  and  $\Delta M2$  are the error bars for respectively the 20.7 and 37.8 meter baselines.

$\lambda$	M1	$\Delta M1$	M2	$\Delta M2$
6538	1.	0.165	-	-
6542	0.980	0.171	0.960	0.258
6546	0.883	0.149	1.020	0.278
6550	0.828	0.148	0.756	0.241
6554	0.828	0.140	0.722	0.201
6558	0.688	0.119	0.422	0.148
6562	0.462	0.091	0.240	0.099
6566	0.624	0.104	0.422	0.148
6570	0.810	0.129	0.722	0.204
6574	0.921	0.148	1.040	0.287
6578	0.921	0.150	0.864	0.248
6582	0.940	0.150	-	-
6586	0.940	0.153	-	-

line force and  $\Phi$  is the mass flux per unit of solid angle.  $F^l$  may be expressed as (Friend & Abbott 1986) :

$$\frac{F^l}{\rho} = \frac{\sigma_e L}{4\pi c r^2} k t^{-\alpha} g(r, v_r, \frac{dv_r}{dr}), \quad (7)$$

Here  $t$  represents an optical depth variable ( $t = \sigma_e \rho v_{th} [\frac{dv}{dr}]^{-1}$ ) and  $k$  and  $\alpha$  are the radiative parameters :  $\alpha$  gives the relative contribution of optically thin to optically thick lines and  $k$  is proportional to the total number of driving lines. The function  $g(r, v, \frac{dv}{dr})$  takes into account the size of the radiating source ("finite disk correction"). All other symbols have their usual meaning:  $L$  is the star's luminosity,  $c$  is the velocity of light,  $\sigma_e$  is the electron scattering coefficient and  $v_{th}$  is the thermal velocity.

The temperature relationship is of the form,

$$T(r) = T_0 \cdot \left(\frac{R}{r}\right)^{2\nu} \quad (8)$$

where  $R$  is the stellar radius. The resulting equation for the expansion is

$$\left[ v_r - \frac{a_0^2}{v_r} \left(\frac{R}{r}\right)^{2\nu} \right] \frac{dv_r}{dr} + \frac{GM(1-\Gamma)}{r^2} = 2 \frac{a_0^2}{R} (1+\nu) \left(\frac{R}{r}\right)^{2\nu+1} + \frac{C \left(\frac{r}{R}\right)^{\nu\alpha}}{r^2} \left( r^2 v_r \frac{dv_r}{dr} \right)^\alpha g(r, v, \frac{dv_r}{dr}) \quad (9)$$

where  $a_0$  is the photospheric speed of sound,  $C$  is an eigenvalue of the equation and is related to the mass flux by the expression

$$C = \frac{\Gamma G M k}{(\sigma_e v_{th} \Phi)^\alpha}. \quad (10)$$

In order to obtain a solution for Eq. (9) one must impose a boundary condition. We have taken the value of the photospheric



density  $\rho_0 = 2.0 \cdot 10^{-11} \text{ g.cm}^{-3}$ . Such a value is suggested by the analysis of Waters et al. (1991). The influence of varying boundary conditions is analysed elsewhere (Araújo 1994). Concerning the radiative parameters we have adopted  $\alpha = 0.5$  and  $k = 0.3$ . These are typical values for early Be stars (Poe & Friend 1986; Araújo & Freitas Pacheco 1989; Owocki et al. 1994). Our numerical solutions yield  $\Phi_{pole} = 1.7 \cdot 10^{-9} M_{\odot} \text{ yr}^{-1} \text{ sr}^{-1}$  and  $V_0 = 0.11 \text{ kms}^{-1}$ . Using a “ $\gamma$ -law” velocity profile of the type:

$$v_r(r, \theta = 0) = V_0(0) + [V_{\infty}(0) - V_0(0)](1 - \frac{R}{r})^{\gamma} \quad (11)$$

leads to a terminal velocity of  $V_{\infty}(0) = 2016 \text{ kms}^{-1}$  and  $\gamma = 0.86$ . The implication of this result will be described in the following section.

#### 4. The parametrized model

To obtain solutions at all stellar latitudes we introduce a parametrized model which is constrained by data from the GI2T.

Our main hypothesis is that the envelope is axi-symmetric with respect to the rotational axis. For a detailed discussion of this assumption see Telting et al. (1993) and our discussion in Sect. 6.5. No meridian circulation is allowed.

##### 4.1. Velocity and hydrogen density distribution

In order to compute the velocity field and the hydrogen density distribution throughout the envelope we start our calculation with the polar (i.e.  $\theta = 0$ ) values.

The hydrodynamic code gives us:

$$\begin{cases} \Phi_{pole} \\ v_r(r, 0) = V_0(0) + [V_{\infty}(0) - V_0(0)](1 - \frac{R}{r})^{\gamma} \\ \rho(r, 0) = \frac{\Phi_{pole}}{(\frac{r}{R})^2 v_r(r, 0)} \end{cases}$$

We now make the hypothesis that the photospheric density does not depend on the stellar latitude,

$$\rho(R, 0) = \rho(R, \theta) = \rho_0. \quad (12)$$

This condition leads to optical depths that increase from the pole to the equator (see also Koninx & Hearn 1992; Blomme et al. 1991).

Furthermore we adopt the following expression for the mass flux:

$$\Phi(\theta) = \Phi_{pole} + [(\Phi_{eq} - \Phi_{pole}) \sin^{m1}(\theta)], \quad (13)$$

where  $m1$  is the first free parameter which describes the variation of the mass flux from the pole to the equator.

We now introduce the ratio between the equatorial and polar mass flux:

$$C1 = \frac{\Phi_{eq}}{\Phi_{pole}}. \quad (14)$$

The values of  $C1$  are typically between  $10^1$  and  $10^4$  (Lamers & Waters 1987).

Thus Eq. (13) can be rewritten as:

$$\Phi(\theta) = \Phi_{pole}[1 + (C1 - 1) \sin^{m1}(\theta)]. \quad (15)$$

The expansion velocity field is given by:

$$v_r(r, \theta) = V_0(\theta) + [V_{\infty}(\theta) - V_0(\theta)](1 - \frac{R}{r})^{\gamma}, \quad (16)$$

with

$$V_0(\theta) = \frac{\Phi(\theta)}{\rho_0} = \frac{\Phi_{pole}[1 + (C1 - 1) \sin^{m1}(\theta)]}{\rho_0}. \quad (17)$$

We set the value of the equatorial terminal velocity to be typically (Janot-Pacheco et al. 1987; Waters et al. 1988):

$$V_{\infty}(eq) \sim 100 - 500 \text{ kms}^{-1}. \quad (18)$$

The second free parameter  $m2$  is introduced in the expression of the terminal velocity as a function of the stellar latitude:

$$V_{\infty}(\theta) = V_{\infty}(pole) + [V_{\infty}(eq) - V_{\infty}(pole)] \sin^{m2}(\theta). \quad (19)$$

Finally by combining Eqs. (15) (16) and (17) we obtain the expression of the radial component of the velocity

$$\begin{aligned} v_r(r, \theta) = & \frac{\Phi_{pole}[1 + (C1 - 1) \sin^{m1}(\theta)]}{\rho_0} + \\ & + (V_{\infty}(pole) + [V_{\infty}(eq) - V_{\infty}(pole)] \sin^{m2}(\theta) - \\ & - \frac{\Phi_{pole}[1 + (C1 - 1) \sin^{m1}(\theta)]}{\rho_0}) (1 - \frac{R}{r})^{\gamma}. \end{aligned} \quad (20)$$

Note that Eq. (20) combines  $C1$ ,  $V_{\infty}(eq)$  and the two free parameters  $m1$  and  $m2$ .

The rotational velocity field throughout the envelope is assumed to be Keplerian according to:

$$v_{\phi}(r, \theta) = \chi \left( \frac{GM(1 - \Gamma)}{R} \right)^{1/2} \sin\theta \left( \frac{R}{r} \right)^{1/2}, \quad (21)$$

where  $\chi$  is the ratio between rotational and critical “break-up” velocities.

Finally the density distribution in the envelope is given by the equation of mass conservation:

$$\rho(r, \theta) = \frac{\Phi(\theta)}{(\frac{r}{R})^2 v_r(r, \theta)}. \quad (22)$$

#### 4.2. The statistical equilibrium

The envelope of  $\gamma$  Cas is assumed to be formed by pure hydrogen atoms which have six bound levels. We have computed the ionization-excitation equation by using Sobolev's approximation (Sobolev 1960):

$$n_i \left( \sum_{k=1}^{i-1} A_{ik} \beta_{ki} + B_{ic} \rho_{ic} \right) = \sum_{k=i+1}^{\infty} n_k A_{ki} \beta_{ik} + n_e^2 C_i(T_e), \quad (23)$$

where the escape probability  $\beta_{ik}$  is given by:

$$\beta_{ik} = \frac{1}{4\pi} \int \beta_{ik}^o (1 - e^{-1/\beta_{ik}^o}) d\Omega, \quad (24)$$

with

$$\beta_{ik}^o = \frac{1}{2u} \frac{dv}{ds} \frac{1}{\alpha_{ik}}, \quad (25)$$

where  $u$  is the mean thermal velocity of atoms,  $\frac{dv}{ds}$  is the line of sight velocity gradient and  $\alpha_{ik}$  is the absorption coefficient of the line.

The notation employed in the statistical equilibrium equation is the usual one, for more details see SA. The recombination coefficient  $C_i(T_e)$  which appears in the ionization-excitation equation depends on the temperature distribution. We have adopted:

$$T(r) = T_{\text{eff}} \left( \frac{R}{r} \right)^{1/2}, \quad (26)$$

with  $T_{\text{eff}} = 25000$  K.

In Sect. 7.5, we consider briefly an isothermal model for the envelope to illustrate how the properties of the envelope depend on the assumed temperature structure.

The solutions for the envelope were found from a model-grid of  $170 \times 90 \times 71$  points (respectively for the radial, latitudinal and azimuthal directions) which corresponds to a maximal extent of 40 stellar radii. For each point we use a standard calculation method. We start with the LTE populations for each level and we update populations until we achieve convergence (For more details also see SA).

#### 4.3. Discussion on the Sobolev approximation used in our modelling

One of the major limitation of our modelling is the use of the Sobolev approximation. Since, the problem of radiative wind was treated in the CAK framework the Sobolev approximation was naturally used for modelling both the transfer and line formation. We know that in a spherically symmetric, rapidly expanding wind, the Sobolev approximation for the treatment of line formation is a good one. It is not obvious that the same applies to our system, especially in the equatorial regions and close to the star where the rotation dominates and where the density is large. In these regions there can be multiple resonance points

along a given ray, so that absorption of line radiation produced upstream can occur at a distant point downstream. This effect can be aided by the finite width of the local absorption coefficient due to thermal motions. Furthermore, in a differentially rotating flow, where the rotational speeds are supersonic, turbulence of some form will be generated. The cascade of the energy in this turbulent flow to smaller scales will lead ultimately to an even wider absorption coefficient, and thus more overlap in velocity or frequency space of widely separated points on the same ray through the envelope. Nevertheless, we cannot determine the magnitude of these effects in our model without doing a completely different calculation.

### 5. The “best model” for $\gamma$ Cas

#### 5.1. The method for fitting the free parameters

In order to find the best values for the equatorial to polar mass loss C1, the equatorial terminal velocity  $V_{\infty}(eq)$ , and the parameters  $m1$  and  $m2$ , we first start with a mass loss which is in good agreement with the values given by Lamers & Waters (1987). They have suggested mass loss rates in the range of  $10^{-9}$  to  $10^{-7} M_{\odot} \text{ yr}^{-1}$ . Next we reproduce the  $H\alpha$  line profile and compare it to the profile measured by the GI2T. Finally we refine the model by comparing the theoretical visibility curves to those obtained from GI2T data following the visibility reduction described in Sect. 2.3.

#### 5.2. The values obtained

The ratio C1 was found to be 30 which corresponds to an equatorial mass flux of  $5.1 \cdot 10^{-8} M_{\odot} \text{ yr}^{-1} \text{ sr}^{-1}$  and taking  $m1 = 6.0$ , then leads to a global mass loss rate of  $\dot{M} = 3.2 \cdot 10^{-7} M_{\odot} \text{ yr}^{-1}$ . This large value compares well with those given by Lamers & Waters (1987) who found  $\dot{M}$  between  $2.5 \cdot 10^{-8}$  and  $5 \cdot 10^{-7} M_{\odot} \text{ yr}^{-1}$  for  $\gamma$  Cas. This value of  $m1 = 6.0$  corresponds essentially to a mass flux enhancing close to the stellar latitude of  $35^\circ$ . ( $m2 = 0.3$ ) producing a very rapid decrease of the radial velocity from the pole to the equator. Such a value is pertinent for obtaining a  $H\alpha$  full width at half maximum (FWHM) which fits the  $H\alpha$  line profile measured by the GI2T. The equatorial terminal velocity  $V_{\infty}(eq)$  was found equal to  $200 \text{ km s}^{-1}$  needed to simulate a lower expansion at the equatorial latitude. The effects on the expansion and rotational components of the velocity, the mass flux, and the hydrogen density are depicted in Fig. 1. The observable effects of changing the parameter value will be discussed in more detail in Sect. 7. The choice of these parameters enabled us to select the “best”  $\alpha$  for the radiative line force. With  $\alpha = 0.05$  and  $k = 10.5$  we were able to obtain an hydrodynamical solution for the equator which results in a terminal velocity of  $201 \text{ km s}^{-1}$  and an equatorial mass flux of  $4.9 \cdot 10^{-8} M_{\odot} \text{ yr}^{-1} \text{ sr}^{-1}$ . In Sect. 8 we will describe the effects of changing values of  $\alpha$  and  $k$  on our modelling.

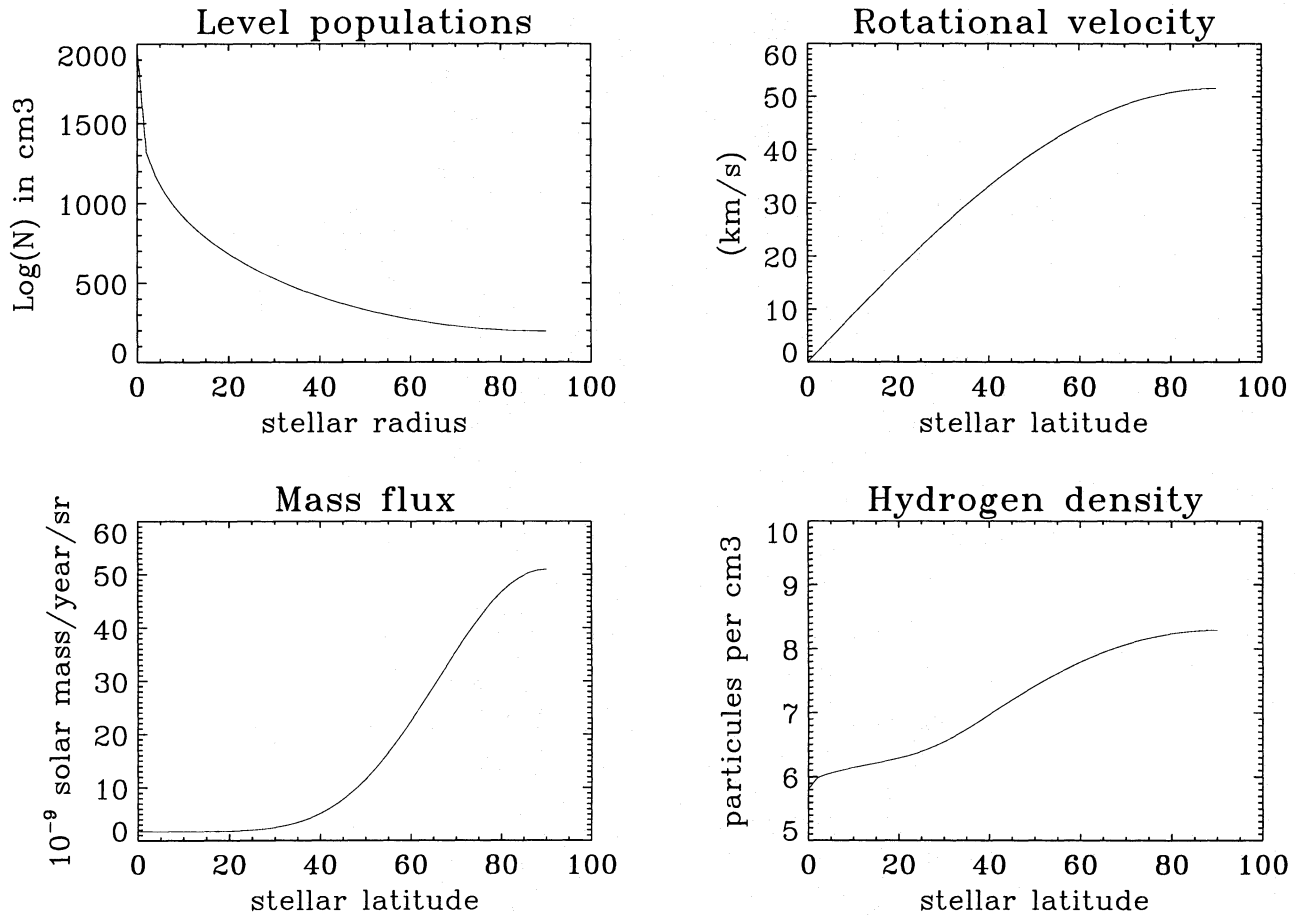


**Fig. 1.** All figures are function of the stellar latitude. Upper left: expansion velocity at 40 stellar radii, upper right: rotational velocity at 40 stellar radii, lower left: mass flux in unit of  $10^{-9} M_{\odot} \text{ yr}^{-1} \text{ sr}^{-1}$ , lower right: hydrogen density at 40 stellar radii

## 6. Comparison between our model and the GI2T data on $\gamma$ Cas

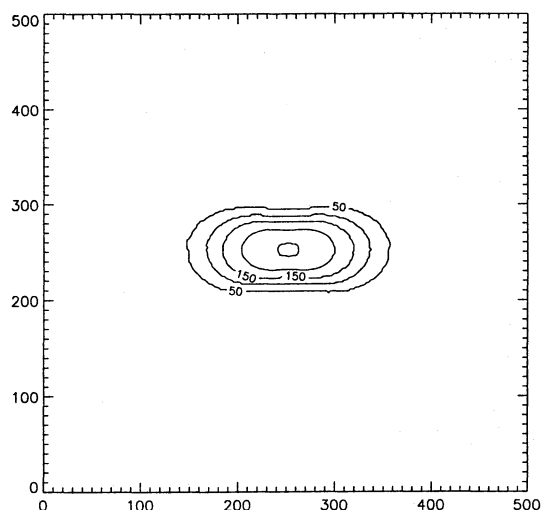
From the parametrized model described above we were able to obtain the hydrogen density distribution across the whole envelope. From Fig. 2 we can see that the hydrogen envelope is markedly flattened towards the equator.

We found that the envelope is almost fully ionized. The population of atomic levels are rapidly increasing from pole to equator (see Fig. 3 and Fig. 4) but most of the hydrogen atoms remain in the fundamental state. Detailed explanation of the dependence of atomic levels with stellar latitude is given by SA.

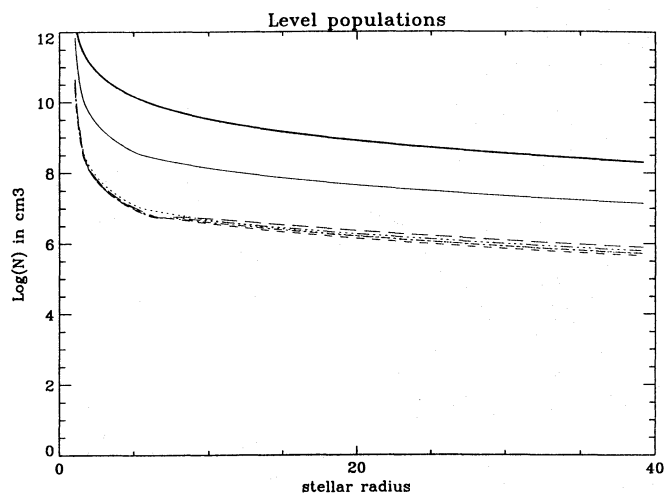
### 6.1. Line profiles

Figure 5 shows the computed (solid line) and measured (dotted line)  $H\alpha$  line profiles. These profiles are normalized to the continuum value ( $I_c$ ). In our line calculation the continuum emission originates from the underlying star which was assumed to radiate as a 25000 K blackbody and also by the continuous emission in the region around  $H\alpha$  from the ionized gas (see Sect. 6.3). The extended wings are mainly due to kinematical effects. The emis-

sion of the blue wing seems to be too strong and the  $V/R < 1$  ratio more pronounced than observed. However, it must be kept in mind that self absorption of the envelope due to a complex (rotating and expanding) velocity field has not been taken into account in our model. Presumably this will reduce the emission from the region projected on the star and will produce an absorption in the blue wing of the emission line. The computed line strength is about 3.7  $I_c$  which is in good agreement with the observed value. We must emphasize that we have verified and compared the  $H\alpha$  line profile obtained with the GI2T with a high resolution profile recorded with the Ondrejov 2 meter telescope (Harmanec & Stefl, private communication) at the same epoch of our interferometric runs. These profiles, albeit using different spectral resolution, were found to be quite similar. The computed  $H\beta$  line profile is also shown in Fig. 6. Its emission is smaller and the photospheric absorption line broadening by the stellar rotation is more noticeable. The computed  $H\beta$  intensity from our model is equal to 1.42  $I_c$ . The derived Balmer decrement is 2.6, which agrees well with the measured value of 2.26 from the GI2T spectra.



**Fig. 2.** Hydrogen isodensity curves seen equator on. The axes are in units of 0.075 stellar radius



**Fig. 3.** Atomic level populations as a function of stellar radius for the equator. Solid thick line:  $n_h$ , solid line:  $n=1$ , dotted:  $n=2$ , dashed:  $n=3$ , dash dot:  $n=4$ , dash dot dot dot:  $n=5$ , long dashes:  $n=6$

### 6.2. $H\alpha$ intensity map and visibility

The measured visibility by the GI2T, as already mentioned in Sect. 2, corresponds to the ratio of the visibility in  $H\alpha$  to the visibility in the nearby continuum. Therefore, in order to compare our model with the data we must first compute the intensity maps in the line and in the continuum.

Next we must Fourier transform these maps independently and compute the ratio of the visibilities for a given spatial frequency. This spatial frequency is obtained by scaling the visibility grid in such a way that one pixel corresponds to the angular diameter of the central star of  $\gamma$  Cas. Figure 7 depicts the theoretical  $H\alpha$  map plotted in iso-intensity levels. The map resembles an ellipsoid with a ratio of minor to major axis of 0.72 for the

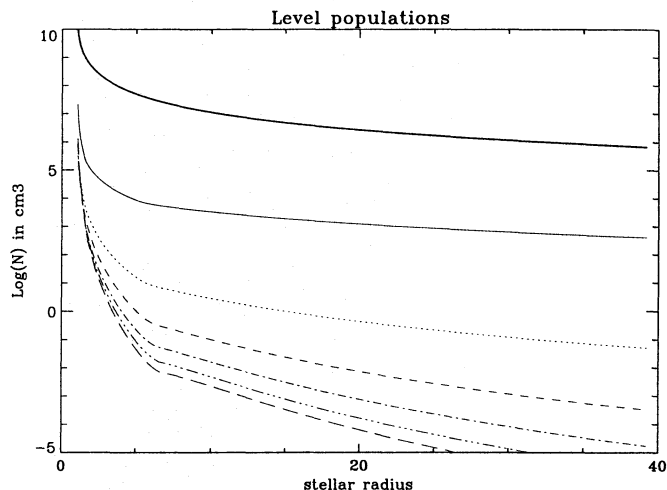


**Fig. 4.** Atomic level populations as a function of stellar radius for the pole. Solid thick line:  $n_h$ , solid line:  $n=1$ , dotted:  $n=2$ , dashed:  $n=3$ , dash dot:  $n=4$ , dash dot dot dot:  $n=5$ , long dashes:  $n=6$

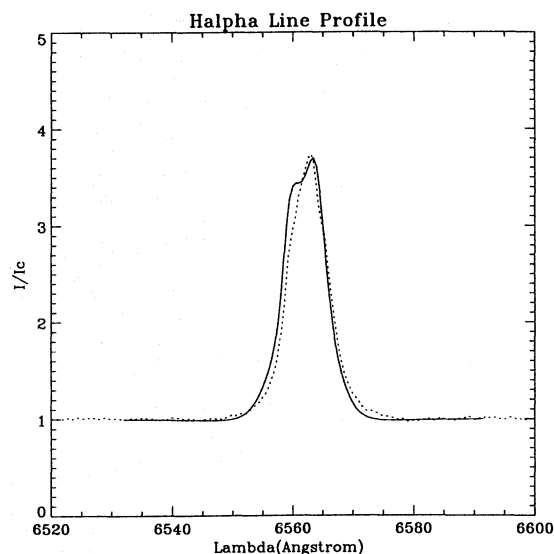


**Fig. 5.** The profile of the  $H\alpha$  line normalized on the local continuum. Solid line: our model, dotted line: GI2T data

level 0.5 which corresponds to  $5 \cdot 10^{-3}$  of the maximum level. This maximum level comes from the stellar emission which is assumed to radiate as a 25000 K black body. The maximum extent of the lower contour is about 80 stellar radii and the major axis of the 0.5 contour corresponds to 17 stellar radii, i.e.  $\sim 4$  mas. This result agrees well with the data of Quirrenbach et al. (1993) who found a ratio of 0.74 from their best model fitting. Our major axis is 12.5 % larger than theirs. The  $H\alpha$  emitting regions are very close to the star and this is due to a hydrogen density which rapidly decreases as a function of the stellar distance. In less than 10 stellar radii the emission drops by a factor of 200. The map was turned to the east by  $20^\circ$  with respect to the north-south direction (which is the vertical axis) in order to fit



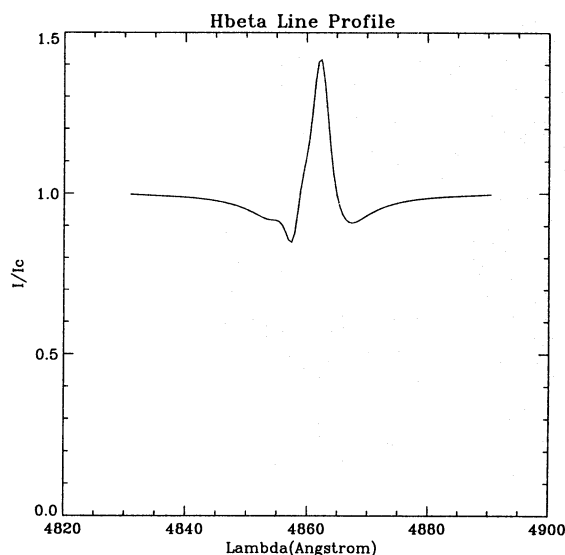


**Fig. 6.** The normalized  $H\beta$  profile computed from our model

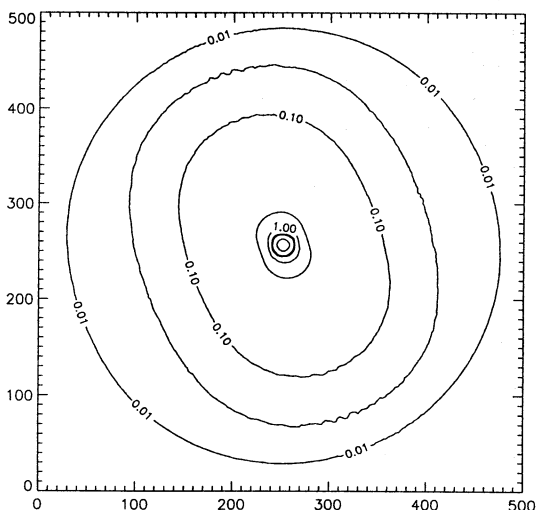


**Fig. 7.**  $H\alpha$  intensity map of  $\gamma$  Cas from the “best model”. Contour levels are respectively 100, 50, 10, 5, 1, 0.5, 0.1, 0.05, 0.01. The axes are in units of 0.075 stellar radius. Note that contour levels 50, 10 and 5 are very close and appeared superimposed in a single “wider ring”

the results of  $21 \pm 5^\circ$  found by Quirrenbach et al. (1993) and its inclination angle was set to  $45^\circ$  with respect to the rotation axis. Figure 8 depicts the corresponding visibility curve. This curve is a cut of the modulus of the 2D Fourier transform of the  $H\alpha$  intensity map in the north-south direction. The rapid decrease of the visibility curve at low spatial frequencies (i.e. down to 0.5) is due to the resolution of the  $H\alpha$  envelope as a function of increasing baseline. The slight decrease for baselines longer than 20 meters is probably due to a partial resolution of the star. We recall that the angular diameter of  $\gamma$  Cas photosphere is taken as 0.45 mas (Ochsenbein & Halbwachs 1982).

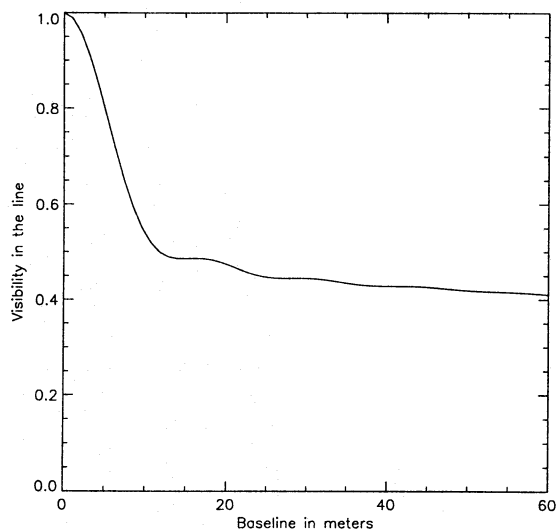


**Fig. 8.** The computed visibility curve of  $\gamma$  Cas in the  $H\alpha$  line as a function of the GI2T baseline (in meters)

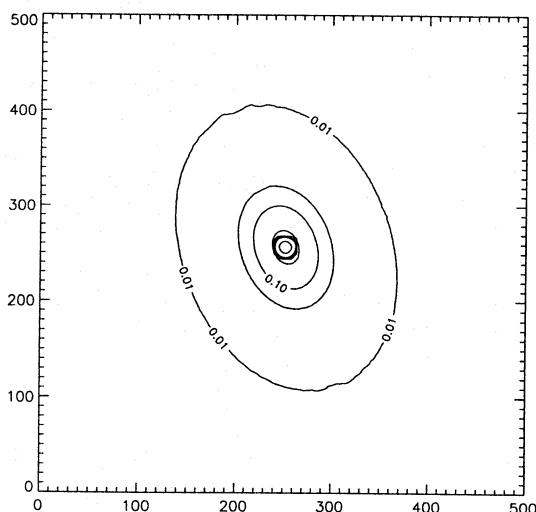


**Fig. 9.** The intensity map of  $\gamma$  Cas in the continuum. Contours levels are respectively 100, 50, 10, 5, 1, 0.5, 0.1, 0.05, 0.01, six pixels correspond to one stellar diameter, i.e. 0.45 mas. Note that contour levels 50, 10, 5 and 1 are very close and appeared superimposed in a single “wider ring”

### 6.3. Continuum intensity map

By using the electron density derived from the resolution of the ionization-excitation equation, we have computed the continuum emission at  $0.65 \mu\text{m}$ . We took into account free-free and free-bound emissions and absorption mechanisms due to free-free and scattering. We find that the envelope contribution to continuum represents 17% of the total flux (star and envelope). Figure 9 depicts the continuum intensity map with the same conventions as for the  $H\alpha$  map. The extension is less important and most of the continuum emission originates within 3–4 stellar radii. We did not simulate the polarization of the photospheric flux by the envelope in the continuum. We might

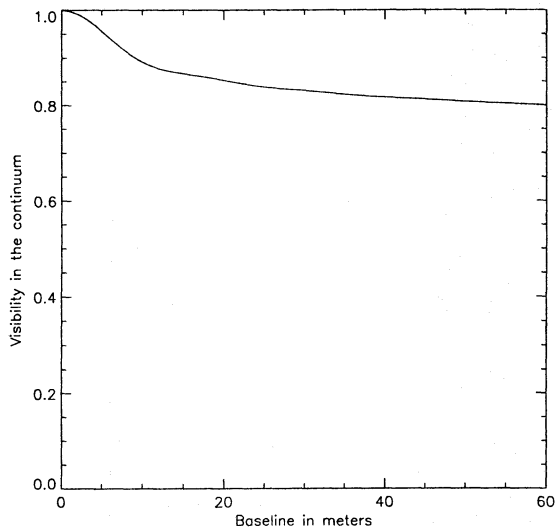


**Fig. 10.** The visibility curve of  $\gamma$  Cas in the continuum as a function of the baseline (in meters) of the GI2T

reasonably speculate that our flattened envelope should produce a significant linear polarization. Recall Waters and Marlborough's conclusion (1992) which established that the bulk of the linear polarization is produced within 2 or 3 stellar radii. Figure 10 shows the visibility curve of the continuum envelope in the north-south direction. From this curve we see that the envelope continuum visibility contributes to 20% of the total visibility curve at large baselines. This is a significant effect and the usual interferometric calibration methods which assume  $\gamma$  Cas as a "point-like" source in the continuum are perhaps not appropriate for this star.

#### 6.4. Relative visibilities

By computing the ratio between the visibility in the  $H\alpha$  line and the visibility in the continuum, we obtain a pseudo-normalized visibility  $M_a$  (see Sect. 2.3.1), which is not an estimate of the absolute visibility at a given spatial frequency. Rather it is a relative visibility in which the effects of atmospheric and instrumental noise have been removed. This is easily understood because the reference visibility in the continuum might correspond to a partially resolved source at high spatial frequencies (i.e. large interferometric baselines). This visibility can be directly compared to the one observed. From Fig. 11 we see that the agreement is better for large baselines than for the two short baselines. This indicates that our model envelope is larger than the observed envelope. It means that although from a purely spectroscopic point of view our "best" model correctly approximates the observed  $H\alpha$  emission profile, the agreement of the corresponding simulated visibility is not as good. A long series of trials for separating the effects of temperature and velocity field structure throughout the envelope could not settle this matter. It would be clarified if we could reach lower spatial frequency visibilities while observing  $\gamma$  Cas. In Sect. 9 we will

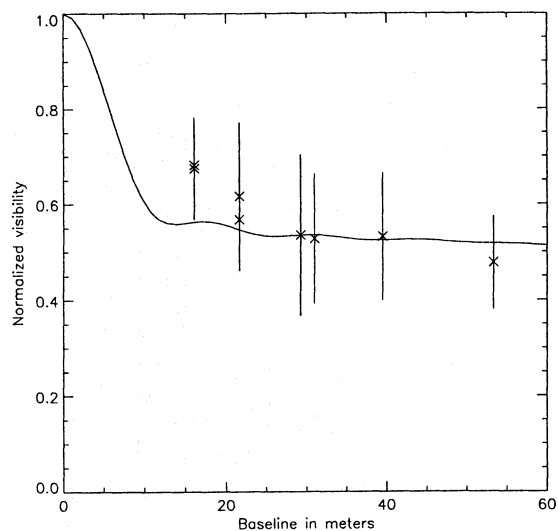


**Fig. 11.** Visibility curve of  $\gamma$  Cas in the  $H\alpha$  line referenced to the visibility in the continuum. Solid line: model, Crosses: GI2T data

discuss in more detail how to overcome the limitation of the short baselines.

#### 6.5. Doppler-shifted intensity maps across the $H\alpha$ line profile

Due to the structure of the velocity field in the envelope, its morphology must strongly depend on the central observational wavelength and bandwidth (see also SA). We have computed intensity maps across the  $H\alpha$  line in order to obtain the change in visibility as a function of wavelength. Each map in Fig. 6.4, Fig. 6.4 and Fig. 7.3 is computed within a bandwidth of 4 Å. This is a minimum bandwidth to obtain a correct signal-to-noise per spectral channel from actual data of the GI2T. The apparent geometry of  $\gamma$  Cas is the same as the one described in Sect. 6.2. From these maps we first note that the emitting region increases in size as a function of Doppler-shift from the blue continuum towards the central wavelength of  $H\alpha$ . For instance at 6532 Å the stellar emission is just visible (Fig. 6.4 upper left) while at 6562 Å the maximal emission extension is observed. The photocenter of each Doppler-shifted map moves along the rotational axis when starting from 6532 Å and ending at 6592 Å. This means that the expansion velocity field plays a major role in the dynamics and also in the morphology of the envelope. For instance if the rotational velocity field was the dominant velocity field, the photocenter would move perpendicularly to the rotational axis when observing from the blue to the red part of the line.

The maps are symmetrical around the central wavelength due to the fact that, as already mentioned, our model is axis-symmetric. A comparison with the visibility obtained from these maps and the GI2T data is shown in Fig. 15 and Fig. 16 for two different baselines. The agreement is good within errors bars of the data but we note a systematic "plateau" present in the data around 6552 Å. This "plateau", which corresponds to a visibility

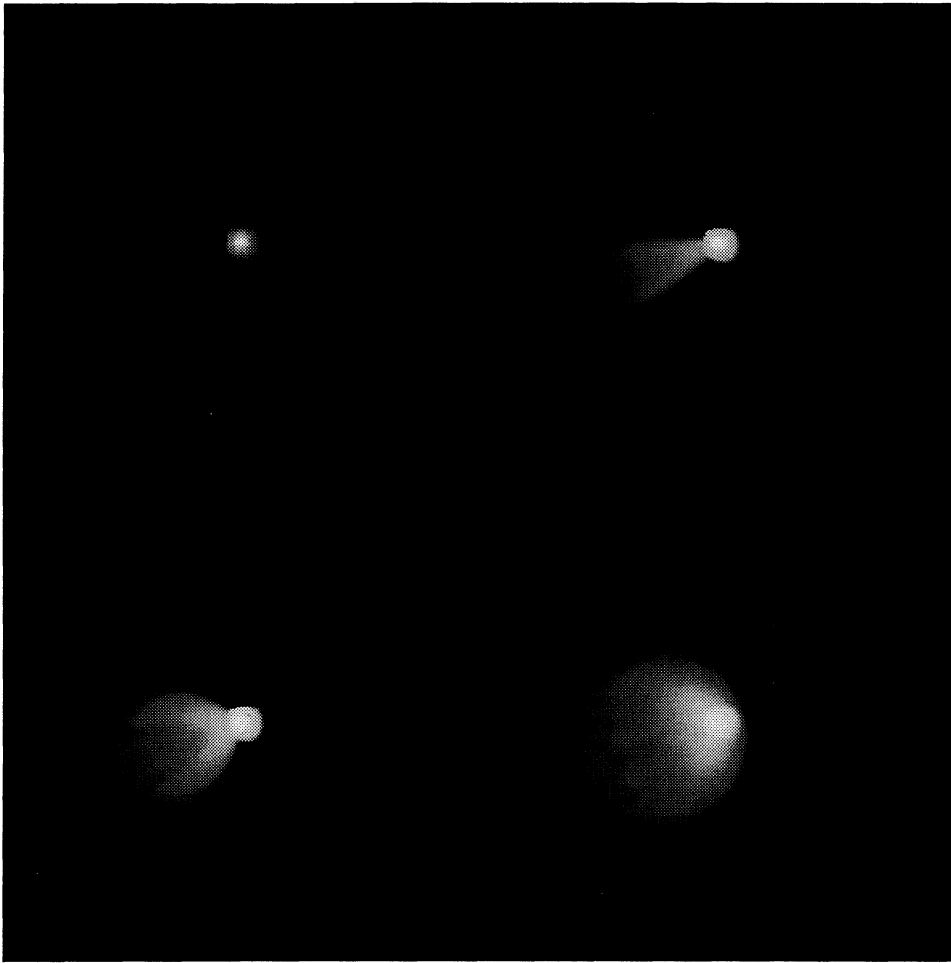


**Fig. 12.** Intensity maps across the  $H\alpha$  line. Each map was computed for a bandwidth of  $4 \text{ \AA}$  but centered at different Doppler-shift across the line. Upper left to lower right maps centered respectively on: 6532, 6542, 6546, 6550  $\text{\AA}$

lower than the predicted one, could suggest that the envelope is not axi-symmetric with respect to the central wavelength. The envelope size in the blue part of the line seems to be systematically larger than in the red part. Such an effect can be produced if a larger density region with higher emission moves towards the observer. Presumably this effect could be related to the material bulk enhanced by a one-armed oscillation in the equatorial disc as suggested by Okazaki (1991) and recently used by Telting & Kaper (1994) for the interpretation of the long-term variability of  $\gamma$  Cas. Another interpretation may be that there is an elliptical envelope which is not exactly centered on the central star.

## 7. Influence of the model parameters

The aim of this section is to examine the range of constraints brought by both the  $H\alpha$  line profiles and the visibility curves on free parameters of our model. This study was conducted by computing a series of different models where we changed one parameter at a time whilst all the others were set to the “best” model. We recall that the best model corresponds to  $m1=6.0$ ,  $m2=0.3$ ,  $C1=30$ ,  $V_\infty=200\text{km/s}$ .

### 7.1. The $m1$ parameter

The parameter  $m1$  defines the variation of the mass flux from the pole to the equator. For instance a larger  $m1$  enhances the mass flux towards the equator making the envelope more disk-like. Figure 17 and Fig. 18 illustrate the mass flux and hydrogen density distribution for  $m1=25.0$ . From Fig. 19 it can be seen that although the FWHM of  $H\alpha$  remains almost unchanged for  $m1=1.0$  and  $m1=25.0$ , the emission strength is notably different. For  $m1=25.0$  a relatively small range of latitude contributes to the line emission and the intensity appears fainter. Moreover, the profile appears double-peaked with  $V/R < 1$  more pronounced. Finally the continuum emitting regions are smaller and the envelope contribution to the continuum is only 10% of the total continuum flux. As a result the plateau (Fig. 20) of the visibility curve is higher because the projected  $H\alpha$  emitting region appears smaller and the stellar contribution to the total  $H\alpha$  emission is larger (see Fig. 20). Finally for  $m1=25.0$  the model produces a lower mass loss of  $1.83 \cdot 10^{-7} M_\odot \text{ yr}^{-1}$ . On the other extreme, a smaller  $m1$  leads to a more spheroidal envelope and the mass flux increases closer to the polar latitudes.

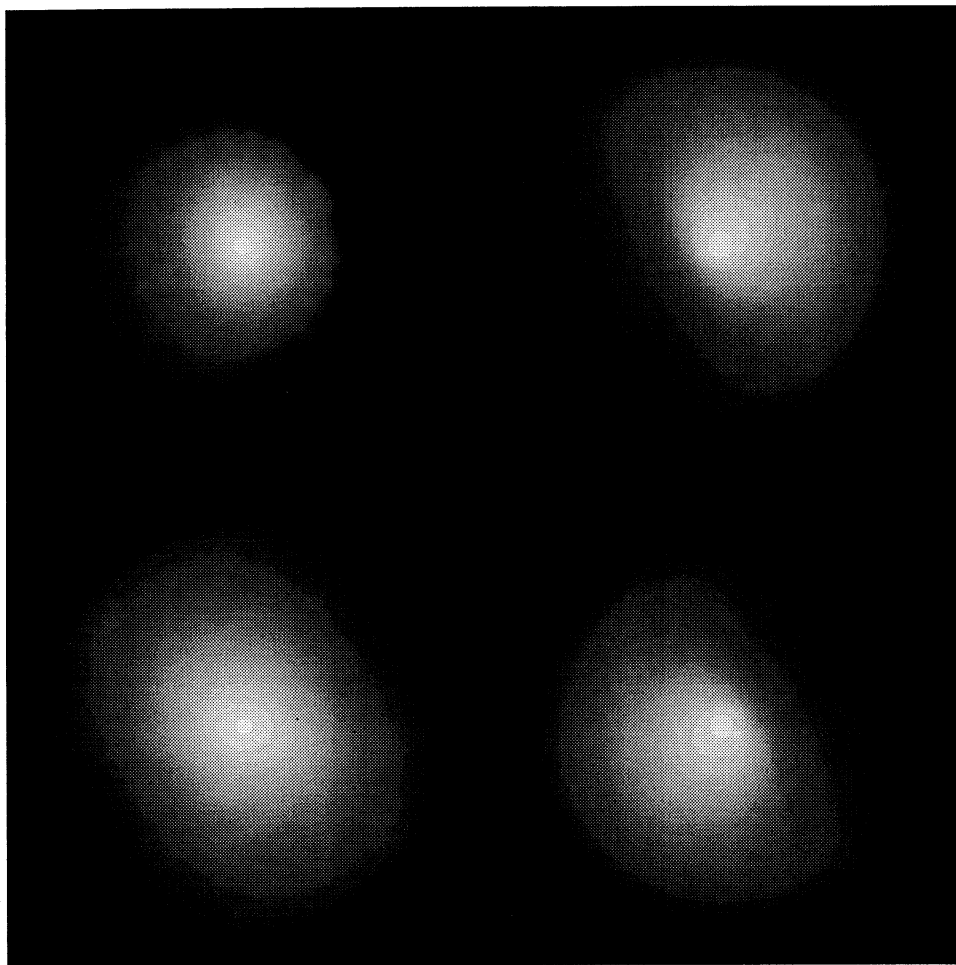


**Fig. 13.** Intensity maps across the  $H\alpha$  line. Each map was computed for a bandwidth of  $4 \text{ \AA}$  but centered at different Doppler-shift across the line. Upper left to lower right maps centered respectively on: 6554, 6558, 6562, 6566  $\text{\AA}$

The  $H\alpha$  line profile has a larger intensity with significantly extended wings (Fig. 19). This is due to a relatively large range of latitude from the pole to larger latitudes, which dominates the emission at line center. The most important effect is an increase of the envelope continuum emission which represents more than 40% of the total continuum emission. This results in a relative visibility curve which increases at higher spatial frequencies (longer baselines) (see Fig. 20).

### 7.2. The $m_2$ parameter

The  $m_2$  parameter has an effect primarily on the envelope kinematics. When  $m_2=1.0$  the expansion velocity decreases more slowly with increasing stellar latitude (Fig. 21). This produces an effect on the  $H\alpha$  line profile so that it appears with a double-peaked shape and extended wings up to  $1000 \text{ km s}^{-1}$ . This is purely a kinematical effect: there is more matter which moves at large velocities and due to the Doppler-effect contributes to the emission in the wings of the line. A smaller  $m_2$  value produces a very fast decrease of the expansion velocity and also a line profile with very steep edges and a larger FWHM. We can no-

tice from the profile (Fig. 22), the presence of the photospheric absorption line broadening by the stellar rotation. Both the envelope continuum and  $H\alpha$  intensity maps remain unchanged for  $m_2=0.1$  or  $m_2=1.0$

### 7.3. The $C1$ parameter

$C1$  is not really a free parameter because it is constrained by the mass loss inferred from IR observations which, as already mentioned, lies between  $2.5 \cdot 10^{-8}$  and  $5 \cdot 10^{-7} M_{\odot} \text{ yr}^{-1}$  (Lamers & Waters 1987). With  $C1=60$ , we obtained a too large mass loss of  $6.2 \cdot 10^{-7} M_{\odot} \text{ yr}^{-1}$ . The line profile is similar to the  $m_1=1.0$  case and is due, in both cases, to the larger contribution of the polar regions (Fig. 23). It also produces a higher visibility but quite different from the  $m_1=1.0$  case (Fig. 24). We must stress the importance of this. It shows, that from a spectroscopic point of view, computed  $H\alpha$  lines with roughly similar profiles can be either obtained from two distinct physical effects: polar to equatorial mass flux which starts to increase close to the polar latitude, or a larger mass flux ratio. From the interferometric



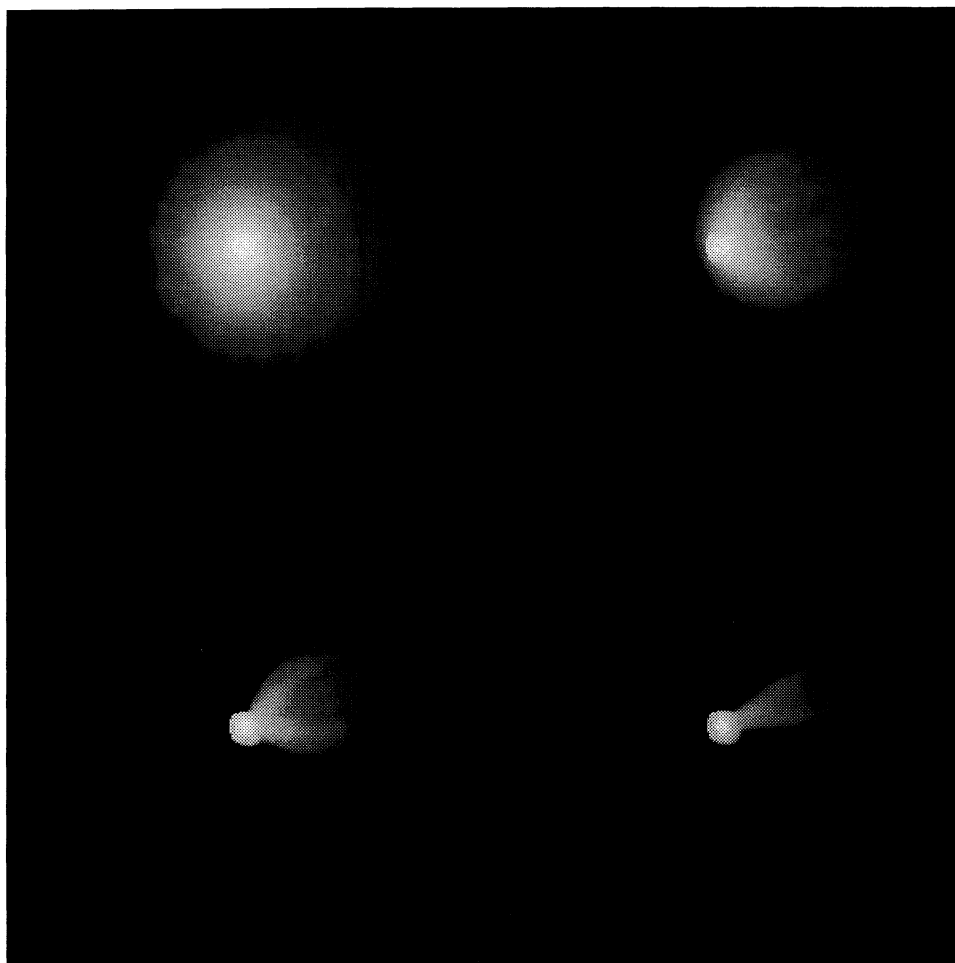


**Fig. 14.** Intensity maps along the  $H\alpha$  line profile. Each map was computed with a bandwidth of  $4 \text{ \AA}$ . Upper left to lower right respectively: 6570, 6574, 6578, 6582  $\text{\AA}$

measurement it is clear that the emitting object and corresponding visibility curves of these cases are quite different.

#### 7.4. The terminal velocity parameter

As for the C1 parameter, the terminal velocity is not a totally free parameter. Janot-Pacheco et al. (1987) and Waters et al. (1988) found a terminal velocity around a few hundred  $\text{km s}^{-1}$ . From our model we find that the terminal velocity must be close to  $200 \text{ km s}^{-1}$  in order to fit the  $H\alpha$  line profile measured by the GI2T. A higher terminal velocity produces a line profile which is excessively broadened, while a velocity of  $100 \text{ km/s}$  produces a line profile both narrower and more intense than the observed profile (Fig. 25). Again the visibility curves are not sensitive to the terminal velocity.

#### 7.5. An isothermal model

In order to examine the influence of the temperature distribution we have computed a model with a constant temperature distribution of  $0.8 T_{eff}$ , i.e.  $20000 \text{ K}$ . The other parameter values are

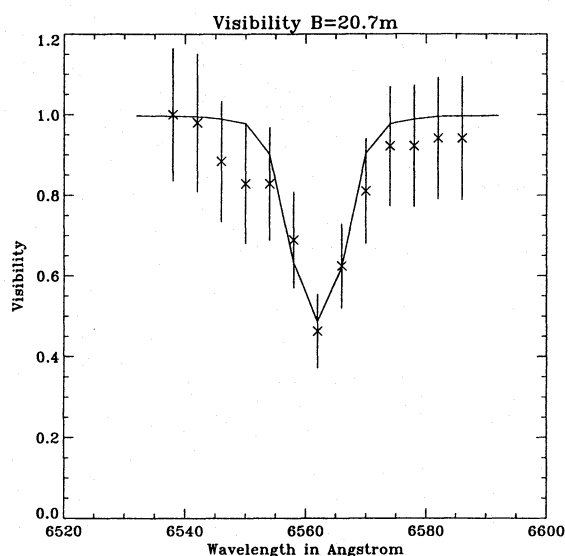


**Fig. 15.** Visibilities corresponding to the Doppler-shifted maps across the  $H\alpha$  line profile for the 20.7 meter baseline. Solid line: model, crosses: actual data from the GI2T

taken from the “best” model. We found that the population of the levels is, for a given stellar radius, lower by a factor 10 compared to the “best” model. In fact this is due to the ionization which increases with increasing temperature and also makes the number of neutral hydrogen atoms lower. This produces a lower intensity of the  $H\alpha$  line profile but does not change the visibility curve.

Table 5 summarizes the different range of parameters estimated from our modelling of  $\gamma$  Cas, as discussed in this section.

**Table 5.** Ranges allowed for the parameters values

Parameter	“best” model	Allowed range
$m1$	6.	$3. < m1 < 9.$
$m2$	0.3	$0.1 < m2 < 0.8$
$C1$	30.	$15. < C1 < 50.$
$V_\infty$	200.	$150. < V_\infty < 250.$

## 8. The physics of the equatorial plane

It is generally believed that Be stars exhibit a slow radial expansion in the equatorial plane. On the other hand most authors infer a large mass loss in this region on the basis of the IR excess (see Waters 1986). Our results confirm this high mass loss for  $\gamma$  Cas. From a detailed reconstruction of  $H\alpha$  line profile and visibility curve we obtain an average terminal velocity of  $V_\infty \sim 200 \text{ km s}^{-1}$  and a mass loss rate of  $\dot{M} \sim 5 \cdot 10^{-8} M_\odot \text{ yr}^{-1} \text{ sr}^{-1}$ . The question which arises naturally is which mechanism may produce an expansion with such characteristics. Classical radiative wind models (driven mostly by optically thick lines) seem ruled out since they lead to terminal velocities of the order of a thousand  $\text{kms}^{-1}$ . In addition these high velocities are attained within a few stellar radii.

A few years ago it was suggested that a radiative wind driven essentially by optically thin lines is more appropriate for the envelope of Be stars: Lamers (1986); Boyd & Marlborough (1991); Lamers & Pauldrach (1991). Recently Araújo et al. (1994) developed a “latitude-dependent” model, in which the relative contribution of optically thick lines decreases from the pole to the equator. However, due to numerical difficulties, they could not obtain solutions for values of the radiative parameter  $\alpha$  lower than 0.4. (Recall that  $\alpha = 0.0$  for a wind driven uniquely by thin lines and  $\alpha = 1.0$  for an expansion driven entirely by thick lines). In a recent work Chen & Marlborough (1994) encountered similar difficulties.

More accurate solutions, for all values of the  $\alpha$  parameter, have been obtained recently by Araújo 1994. In Table 6 and Fig. 26 we show the results of this work applied to  $\gamma$  Cas (Table 1). Acceptable values for the terminal velocity ( $V_\infty \sim 200 \text{ kms}^{-1}$ ) require  $\alpha \sim 0.05$ . This indicates a wind driven almost solely by optically thin lines. On the other hand, the large mass flux implies a value of the  $k$  parameter of about 10. This is an extremely large value, well above those normally estimated. When  $\alpha = 0.0$ ,  $k$  gives simply the ratio between the force due to

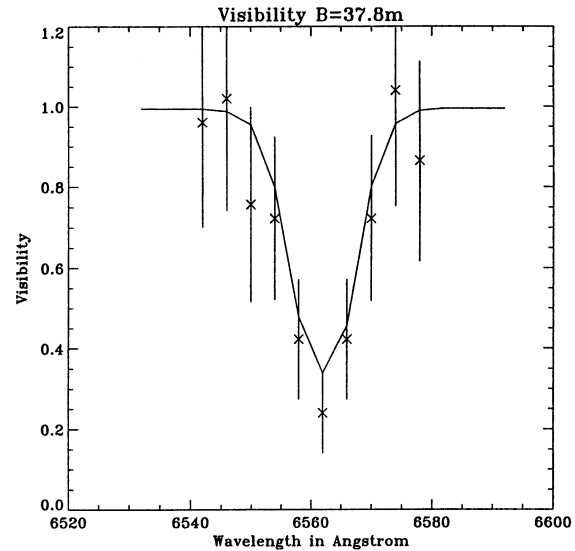


**Fig. 16.** Visibilities corresponding to the Doppler-shifted maps across the  $H\alpha$  line profile for the 37.8 meter baseline. Solid: model, crosses: actual data from the GI2T

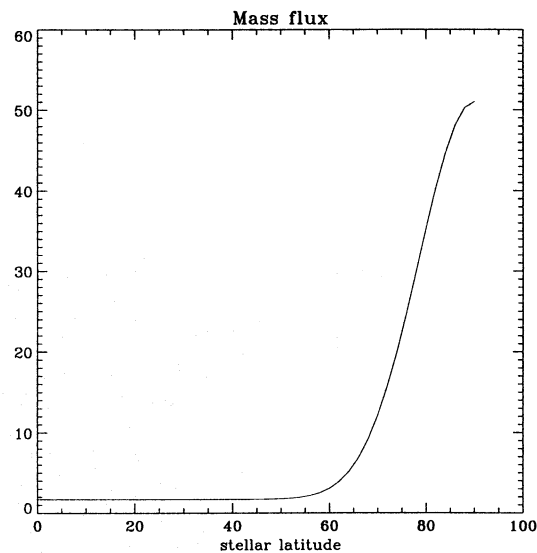


**Fig. 17.** Mass flux as a function of stellar latitude for the  $m1=25$  case

thin lines and that produced by free electrons. Therefore a thin line wind model can well reproduce the equatorial expansion of  $\gamma$  Cas, providing the contribution of these weak lines is about ten times greater than the force produced by the free electrons.

Figure 26 displays the equatorial expansion velocity as a function of stellar radii for different values of  $\alpha$  and  $k$ . Globally, the velocity increases more slowly with decreasing values of  $\alpha$ . The terminal velocity decreases from  $206 \text{ kms}^{-1}$  to  $144 \text{ kms}^{-1}$  for  $\alpha = 0.5$  and  $\alpha = 0.05$  respectively. In a future paper we shall discuss in more detail the numerical resolution of the hydrodynamical equations for a wind driven mainly by optically thin lines.

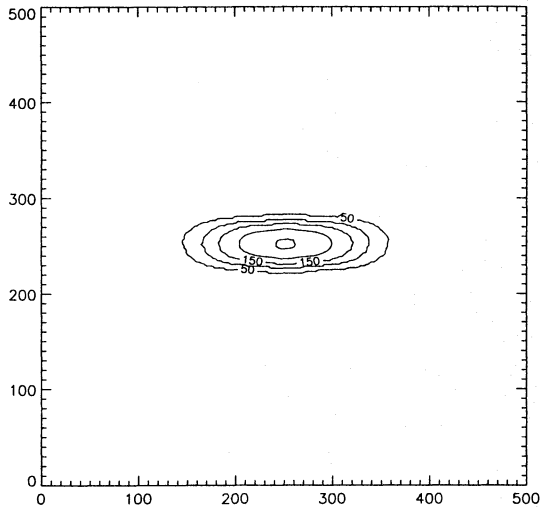


**Fig. 18.** Hydrogen isodensity curves seen equator-on for the  $m1=25.0$  case, six pixels correspond to one stellar diameter, i.e. 0.45 mas

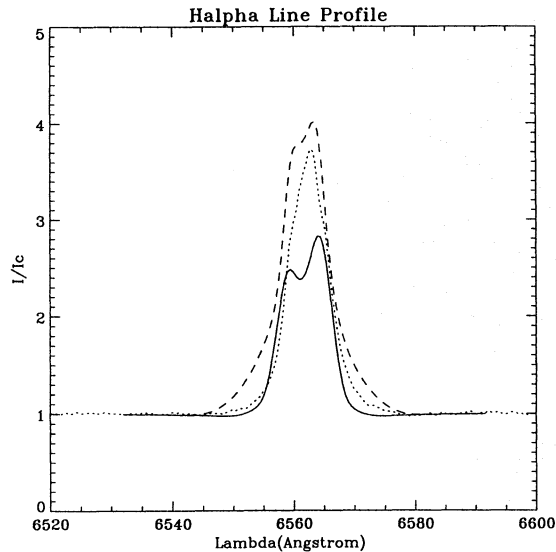


**Fig. 19.** Modeled and observed  $H\alpha$  line profile. Dotted: actual profile from the GI2T, solid: model profile for  $m1=25.0$ , dashed:  $m1=1.0$

## 9. Summary and conclusion

We have described the Be star  $\gamma$  Cassiopeiae in the context of a radiatively driven mechanism for the wind. In order to reproduce both the spectroscopic and interferometric measurements from the GI2T optical interferometer, we have computed a model in which the polar regions are dominated by optically thick lines whereas the wind in the equatorial regions is dominated by optically thin lines. This is the first time that a complete hydrodynamical solution has been obtained for very small values of the radiative parameter  $\alpha$  without the usual numerical difficulties. The computed expansion velocity field is shown to attain a terminal velocity of  $2000 \text{ km s}^{-1}$  in the polar regions whilst not exceeding  $200 \text{ km s}^{-1}$  in the equatorial regions. The rotational velocity field in the envelope is assumed to be Keplerian. The

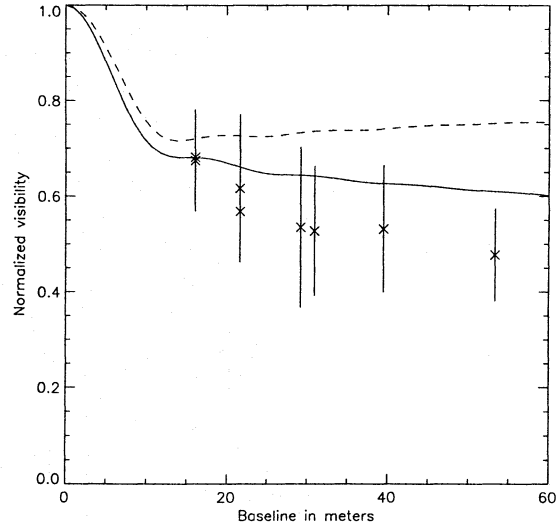


**Fig. 20.** Normalized visibility curve. Solid line:  $m1=25.0$ , dashed line:  $m1=1.0$ , Cross: GI2T data

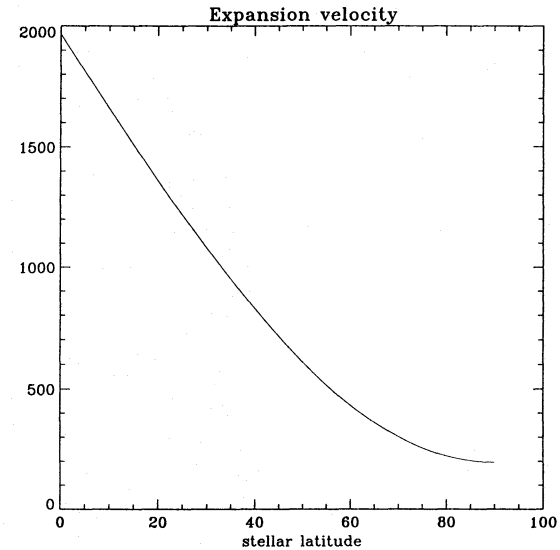


**Fig. 21.** Expansion velocity field as a function of stellar latitude for the  $m2=1$  case

temperature distribution of the form  $\sim r^{-0.5}$  produces a population of the levels which allows us to obtain quite correct line profiles and an almost fully ionized envelope. The resulting electron distribution is responsible for an envelope continuum flux which contributes to 17% of the total continuum emission at red wavelengths. In our case the envelope continuum emission contributes to 20% to the visibility for large baselines. This is an important effect which rules out the usual interferometric calibration method considering the continuum source as “point-like” (Thom et al. 1986; Mourard et al. 1989) at least for  $\gamma$  Cas. Finally, 90% of the  $H\alpha$  emission originates from an ellipsoid with a ratio of minor to major axis of 0.72. This major axis is about 17 stellar radii which corresponds to  $\sim 4$  mas assuming a stellar diameter of 0.45 mas for the stellar photosphere. This

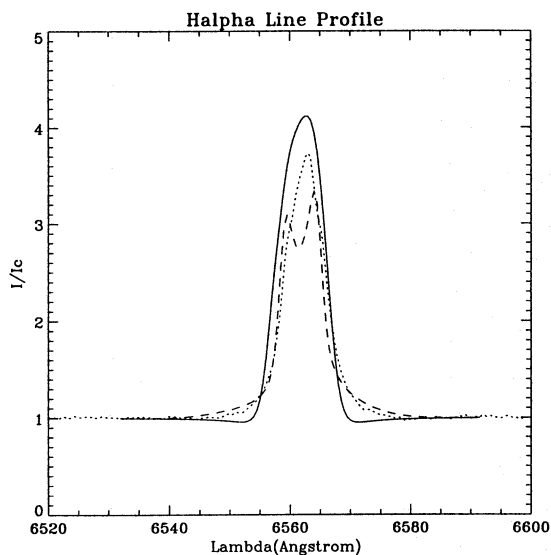


**Fig. 22.** Modeled and observed  $H\alpha$  line profiles. Dotted: actual profile from the GI2T, solid: model profile for  $m_2=0.1$ , dashed:  $m_2=1$

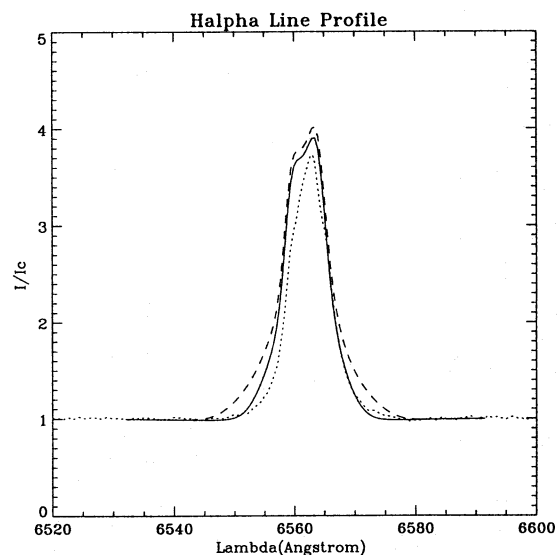


**Fig. 23.** Modeled and observed  $H\alpha$  line profiles. Dotted: actual profile from the GI2T, solid: model profile for  $C_1=60$ , dashed:  $m_1=1$

value is in the same range but larger than those of 3.25 mas found by Thom et al. (1986) and 3.2 mas by Quirrenbach et al. (1993). Unfortunately, due to the limited shortest baseline of the GI2T (11 meters) it is difficult to distinguish between a fast or slowly decreasing of the visibility curve at low spatial frequencies. A possible alternative would be to assume a smaller angular diameter for the photosphere of  $\gamma$  Cas. This is generally estimated as 0.45 mas which corresponds to a distance of 200 parsecs. By taking an angular photospheric diameter of 0.3 mas we simply change the scale of the relative visibilities as a function of spatial frequency without changing the morphology of  $\gamma$  Cas computed by our “best” model. Thereby the fit of our theoretical relative visibilities to the data would improve.

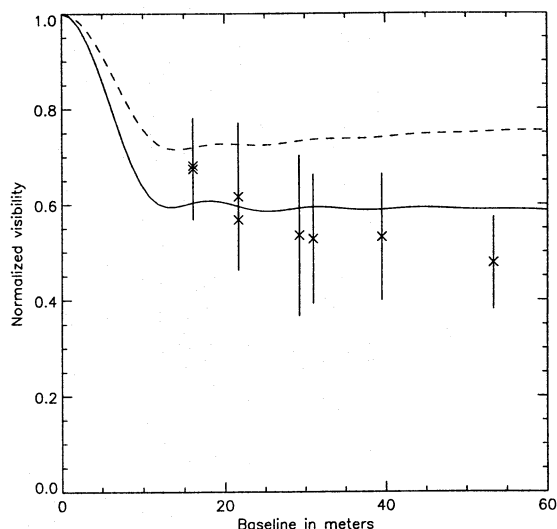


**Fig. 24.** Normalized visibility curve. Solid line:  $C_1=60$ , dashed line:  $m_1=1$ , Cross: GI2T data

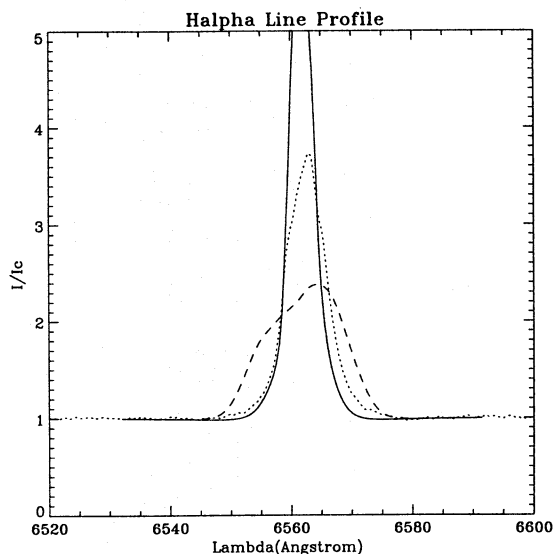


**Fig. 25.** Modeled and observed  $H\alpha$  profiles. Dotted: actual profile from the GI2T, solid: model profile for  $V_\infty=100\text{km/s}$ , dashed:  $V_\infty=400\text{km/s}$

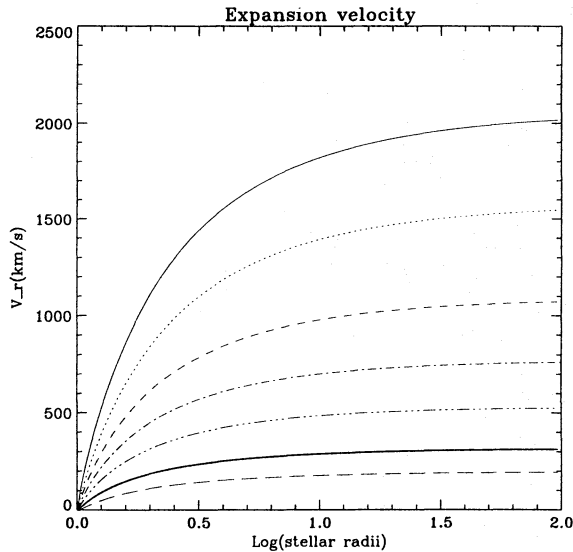
The visibility curves along the  $H\alpha$  profile are in good agreement with the computed ones. However our data shows a larger emitting region in the blue part of the line, which our axi-symmetric model cannot reproduce.

For the first time a model that agrees well with both spectroscopic and interferometric measurements in the Balmer lines and the continuum is proposed. Nevertheless it needs further improvements in order to account for non-axisymmetrical features, emission in UV lines, other spectral regions, and polarization.



**Table 6.** Mass fluxes and terminal velocities as a function of  $\alpha$  and  $k$  values

$\theta$	$\alpha$	$k$	$\Phi$ ( $M_{\odot} / \text{y.sr}$ )	$V_{\infty}$ (km/s)
0	0.5	0.3	$1.7 \cdot 10^{-9}$	2016
90	0.5	0.3	$2.9 \cdot 10^{-9}$	1545
	0.4	0.3	$3.6 \cdot 10^{-10}$	1064
	0.4	0.6	$2.0 \cdot 10^{-9}$	1071
	0.3	0.6	$1.2 \cdot 10^{-10}$	753
	0.3	1.5	$2.6 \cdot 10^{-9}$	761
	0.2	1.5	$5.6 \cdot 10^{-11}$	517
	0.2	3.5	$3.8 \cdot 10^{-9}$	524
	0.1	3.5	$5.0 \cdot 10^{-12}$	304
	0.1	7.0	$4.9 \cdot 10^{-9}$	312
	0.05	7.0	$1.6 \cdot 10^{-11}$	189
	0.05	9.0	$2.4 \cdot 10^{-9}$	194
	0.05	10.5	$4.9 \cdot 10^{-8}$	201
	0.03	11.0	$3.3 \cdot 10^{-8}$	144

**Fig. 26.** Expansion velocity as a function of stellar latitude. The values of  $\alpha$  and  $k$  are respectively (from top to bottom):Polar latitude: solid line:  $\alpha=0.5, k=0.3$ 

At the equator: dotted: 0.5, 0.3; dashed: 0.4, 0.6; dash dot: 0.3, 1.5; dash dot dot: 0.2, 3.5; solid thick: 0.05, 10.5; long dashes: 0.05, 9.0

**Acknowledgements.** We thank P. Harmanec and S. Stefl for the H $\alpha$  spectrum obtained at the Ondrejov Observatory. We also thank A. Labeyrie and P. Lawson for many helpful suggestions and careful reading of the manuscript. We are grateful to J. Pacheco for several fruitful discussions on the physics of Be stars. The useful remarks of the referee J. M. Marlborough are also greatly acknowledged by the authors. F.X. de Araújo acknowledges CNPq (Brazil) for post-doctoral fellowships (20 2091/91.0).

## References

- Araújo, F.X., Freitas Pacheco, J.A. 1989, MNRAS, 241, 543
- Araújo, F.X., Freitas Pacheco, J.A., Petrini, D. 1994, MNRAS, 267, 501
- Araújo, F.X. 1994, A&A, in press.
- Bjorkman, J.E., Cassinelli, J.P. 1993, ApJ, 409, 429
- Blazit, A. 1987, Thèse de Doctorat, Université de Nice (France)
- Blomme, R., Vanbeveren D., Van Rensbergen W. 1991, A&AS, 241, 479
- Boyd, C.J. and Marlborough, J.M. 1991, ApJ, 369, 191
- Castor, J.I., Abbott, D.C., Klein, R.I. 1975, ApJ 195, 175
- Chen, H., and Marlborough, J. M. 1994, ApJ, 427, 1005
- Clarke, D. 1990, A&A, 227, 151
- Dachs, J., Hanuschik, R., Kaiser, D. and Rohe, D. 1986, A&A, 159, 276
- Doazan, V., Thomas, R.N., and Barylak, M. 1986, A&A, 159, 75
- Doazan, V. 1987, IAU Colloquium 92, ed. A. Sletteback and T.P. Snow, Cambridge, Cambridge University Press, p 279
- Doazan, V. 1982, in B stars with and without emission lines, eds A. Underhill, V. Doazan, NASA SP- 456, p 277
- Floquet, M., Hubert, A.M., Janot-Pacheco, E., Mekkas, A., Hubert, H., and Leister, N.V. 1992, A&A, 264, 177
- Foy, R. 1988, "The photon counting camera CP 40", in Robinson L. B., editor, Instrumentation for Ground-Based Optical Astronomy, Present and Future, 589, New-York, Springer-Verlag.
- Friend, D.B., Abbott, D.C. 1986, ApJ, 311, 701
- Hubert, A.M. 1994, Symposium IAU 162, ed. H. Henrichs, L. Balona, and J.M. Le Contel, Kluwer Academic Publishers, p 341
- Janot-Pacheco, E., Motch, C. and Mouchet, M. 1987, A&A, 177, 81
- Koninx, J.P.M., and Hearn, A.G. 1992, A&A, 263, 208
- Lamers, H.J.G.L.M. 1986, A&A, 159, 90
- Lamers, H.J.G.L.M., Waters, L.B.F.M. 1987, A&A, 182, 80.
- Lamers, H.J.G.L.M., Pauldrach, A.W.A. 1991, A&A, 244, L5
- Marlborough, J. M. 1987, IAU Colloquium 92, ed. A. Slettebak and T.P. Snow, Cambridge, Cambridge University Press
- Mourard, D., Bosc, I., Labeyrie, A., Koechlin, L. and Saha, S. 1989, Nature, Vol 342, 520
- Mourard, D., Bosc, I., Blazit, A., Bonneau, D., Merlin, G., Morand, F., Vakili, F., Labeyrie, A. 1994a, A&A, 283, 705
- Mourard, D., Tallon-Bosc, I., Rigal, F., Vakili, F., Bonneau, D., Morand, F., and Stee, Ph. 1994b, A&A, 288, 675
- Ochsenbein, F., and Halbwachs, J.L., A&AS, 47, 523
- Okazaki, A.T. 1991, PASJ, 43, 75
- Owoc, S.P., Cranmer, S.R. and Blondin, J.M. 1994, ApJ, in press
- Pavloski, K., 1987, Ap&SS, 134, 317
- Percheron, I., Rabbia, Y., and Vakili, F. 1994, A&A, submitted
- Poe, C.H., Friend, D. 1986, ApJ, 311, 317
- Poeckert, R., and Marlborough, J. M. 1978, ApJ 220, 940
- Quirrenbach, A., Hummel, C.A., Buscher, D.F., Armstrong, J.T., Mozurkewich, D., and Elias II, N.M. 1993, ApJ, 416, L25
- Quirrenbach, A., Buscher, D.F., Mozurkewich, D., Hummel, C.A., and Armstrong, J.T. 1994, A&A, 283, L13
- Slettebak, A., and Snow, T.P. 1978, ApJ, 224, L127
- Slettebak, A. 1982, ApJS, 50, 55
- Slettebak, A. 1988, PASP, 100, 770
- Sobolev, V.V. 1960, Moving envelopes of star, Harvard University Press, Cambridge, Mass.
- Stee, Ph., and Araújo, F.X. 1994, A&A, in press
- Telting, J. H., Waters, L.B.F.M, Persi, P., and Dunlop S.R. 1993, A&A, 270, 355
- Telting, J. H., and Kaper, L. 1994, A&A, 284, 515
- Thiebaud, E. 1994, A&A, 284, 340
- Thom, C., Granes, P., Vakili, F. 1986, A&A, 165, L13

- Vakili, F., Bonneau, D., Lawson, P., Merlin, G., Mourard, D., Stee, P., Tallon-Bosc, I., and Vallée, F. 1994, "Amplitude and Intensity Spatial Interferometry II", ed. J.B. Breckinridge, vol. 2200, SPIE, Hawaii
- Walker, M.F. 1953, ApJ, 118, 481
- Waters, L.B.F.M. 1986, A&A, 162, 121
- Waters, L.B.F.M., Coté, J., Lamers, H.G.J.L.M. 1987, A&A, 185, 206
- Waters, L.B.F.M., Taylor, A.R., van den Hanvel, E.P.J., Habets, G.M.H.J. and Persi, P. 1988, A&A, 198, 200
- Waters, L.B.F.M., van den Veen, W.E.C.J., Taylor, A.R., Marlborough, J. M., and Dougherty, S.M. 1991, A&A, 244, 120
- Waters, L.B.F.M., Marlborough, J. M. 1992, A&A, 253, L25

**Note added in proof:** The authors would like to note that the uncertainties in the measured visibility points, as noted in Figs. 11, 15, 16, 20 and 24 were overestimated by a factor of two and should thus be one half of the size indicated.